

JGR Solid Earth











RESEARCH ARTICLE

10.1029/2023JB027008

Special Section:

Understanding and anticipating Induced Seismicity: from mechanics to seismology

Enhanced Microseismicity During Production Pumping Cessation at the San Emidio Geothermal Field (Nevada, USA) in December 2016

Hao Guo¹ , Clifford Thurber¹ , Ian Warren^{2,3} , Benjamin A. Heath^{1,4} , Matthew Folsom^{5,6}, Hiroki Sone¹ , Neal Lord¹ , John Akerley⁵ , and Kurt L. Feigl¹ 

¹Department of Geoscience, University of Wisconsin-Madison, Madison, WI, USA, ²National Renewable Energy Laboratory, Golden, CO, USA, ³Now at Zanskar Geothermal & Minerals, Inc., Salt Lake City, UT, USA, ⁴Now at National Tsunami Warning Center, Palmer, AK, USA, ⁵Ormat Technologies, Inc., Reno, NV, USA, ⁶Now at Geologica Geothermal Group, Inc., Reno, NV, USA

Key Points:

- We performed a detailed seismic analysis of microseismicity during a short, planned pumping cessation at the San Emidio geothermal field
- The microseismicity likely occurred on critically stressed faults and fractures due to pore pressure increase when production pumping ceased
- There may be a positive correlation between pore pressure increase and microseismic event magnitude

Supporting Information:

Supporting Information may be found in the online version of this article.

Correspondence to:

H. Guo,
hao.guo@wisc.edu

Citation:

Guo, H., Thurber, C., Warren, I., Heath, B. A., Folsom, M., Sone, H., et al. (2023). Enhanced microseismicity during production pumping cessation at the San Emidio geothermal field (Nevada, USA) in December 2016. *Journal of Geophysical Research: Solid Earth*, 128, e2023JB027008. <https://doi.org/10.1029/2023JB027008>

Received 30 APR 2023

Accepted 21 OCT 2023

Author Contributions:

Conceptualization: Hao Guo, Clifford Thurber, Ian Warren, Hiroki Sone, Kurt L. Feigl

Data curation: Hao Guo, Ian Warren, Benjamin A. Heath, Matthew Folsom, Neal Lord, John Akerley, Kurt L. Feigl

Abstract Tectonic activity, geothermal fluids, and microseismic events (MSEs) tend to occur in similar locations as a result of spatiotemporal changes in the subsurface stress state. To quantify this association, we analyze data from a dense seismic array deployed at the San Emidio geothermal field, Nevada for 1 week in December 2016 to coincide with a 19.45-hr shutdown of all injection and production pumping operations. 123 MSEs were detected, of which 101 occurred during the shutdown. The spatial association of the MSEs with the production wells suggests a causal relationship between the production cessation and the MSEs. Here we performed a detailed analysis to investigate reservoir material properties, distribution of seismically activated faults, and local stress state. We determined the hypocenters, magnitudes, and focal mechanisms for the MSEs, P-wave tomographic velocity model, and local stress tensor. The results show that most MSEs occurred near the production wells. Magnitudes fall between -2.2 and 0.0 with larger events located closer to the production wells. Most MSEs occurred within a westward-dipping normal fault zone in the reservoir associated with anomalously low P-wave velocity values. The focal mechanism and stress inversion results show predominantly normal faulting with the maximum horizontal stress oriented north-south. We suggest that the MSEs during shutdown were triggered on pre-existing, small-scale, critically stressed fault patches in the reservoir as the pore pressure increased around the production wells when the production pumping ceased. We interpret the larger MSE magnitudes closer to the production wells as a result of higher pore pressure increase.

Plain Language Summary Microseismic events (MSEs) associated with production and injection of oil, gas, and water have been observed in many locations. In December 2016, a seismic array with 1,302 instruments was deployed at the geothermal field at San Emidio, Nevada, USA to coincide with a 19.45-hr time interval when all pumping operations were temporarily shut down. The seismic network detected 123 MSEs, of which 101 occurred during the shutdown. To understand the physical mechanism driving these MSEs, we perform a detailed seismic and stress analysis with the seismic data collected at San Emidio in 2016. Our analysis includes estimating the hypocentral locations, magnitudes, and focal mechanisms of the microseismic events, forming 3-dimensional images of P-wave velocity via seismic tomography, and calculating the orientations of the principal axes of the local stress tensor. Our results show that most MSEs occurred within a normal fault zone in a fluid-filled reservoir near the production wells. We suggest that the temporary cessation of production pumping increased the pore pressure, decreased the effective stress on the pre-existing, critically stressed fault patches and fractures, and thereby enhanced the microseismicity.

1. Introduction

Seismicity over a range of small to moderate size (magnitude 3 to 6) associated with industrial operations has been observed in oil and gas exploitation sites, wastewater injection operations, and geothermal fields. The primary mechanism is inferred to be stress changes due to active fluid injection and resource production (e.g., Ellsworth, 2013; Keranen & Weingarten, 2018; Segall, 1989; Segall & Fitzgerald, 1998; Zang et al., 2014).

Increases in microseismicity (magnitude less than 3) have also been associated with the temporary cessation of pumping at production wells in geothermal fields. This phenomenon was recently reported at the Brady Hot Springs geothermal field, Nevada, USA (Cardiff et al., 2018). The basic hypothesis is that fluid extraction during

© 2023. The Authors.

This is an open access article under the terms of the [Creative Commons Attribution-NonCommercial-NoDerivs License](https://creativecommons.org/licenses/by-nc-nd/4.0/), which permits use and distribution in any medium, provided the original work is properly cited, the use is non-commercial and no modifications or adaptations are made.

Formal analysis: Hao Guo, Clifford Thurber, Benjamin A. Heath, Matthew Folsom, Hiroki Sone
Funding acquisition: Clifford Thurber, Ian Warren, John Akerley, Kurt L. Feigl
Investigation: Hao Guo, Clifford Thurber, Ian Warren, Matthew Folsom, Neal Lord, John Akerley, Kurt L. Feigl
Methodology: Hao Guo, Clifford Thurber
Project Administration: Ian Warren, John Akerley, Kurt L. Feigl
Resources: Clifford Thurber, Matthew Folsom, Kurt L. Feigl
Software: Hao Guo
Supervision: Clifford Thurber
Validation: Hao Guo, Clifford Thurber, Benjamin A. Heath, Matthew Folsom, Hiroki Sone, Kurt L. Feigl
Visualization: Hao Guo, Matthew Folsom, Kurt L. Feigl
Writing – original draft: Hao Guo
Writing – review & editing: Hao Guo, Clifford Thurber, Ian Warren, Benjamin A. Heath, Matthew Folsom, Hiroki Sone, Neal Lord, John Akerley, Kurt L. Feigl

normal power plant operation inhibits fault slip by reducing pore pressure (P_p) and thereby increasing the effective normal stress on faults, whereas short-term cessations of production promote fault slip by increasing P_p and decreasing the effective stress. Similar correlations between microseismicity and production pumping cessation during planned power plant shutdowns have also been observed at the Kakkonda geothermal field, Japan (Tosha et al., 1998), the Blue Mountain geothermal field, Nevada, USA (Gonzalez et al., 2022; Templeton et al., 2017), and the San Emidio geothermal field, Nevada, USA (Feigl et al., 2022, 2023; Warren et al., 2018).

In December 2016, a dense seismic array was deployed at the San Emidio geothermal field for about 1 week and 123 microseismic events (MSEs) were detected by Warren et al. (2018) (Figure 1). Temporal evolution of the MSEs shows a substantial increase in microseismicity during a 19.45-hr-long shutdown of pumping at all production and injection wells (Figures 1 and 2). A majority of the MSEs during shutdown occurred adjacent to two production wells in the northeastern part of the seismic array (Figure 1), suggesting a direct connection between the MSEs and the cessation of pumping at the production wells.

To understand the spatial distribution and temporal evolution of the stress field at San Emidio, the WHOLES-SCALE project began in 2020 (Feigl et al., 2022). As a part of the WHOLES-SCALE project, we have performed a detailed analysis of the 2016 December seismic data set, including: (a) determining high-precision hypocentral locations, magnitudes, and focal mechanisms for observed MSEs; (b) developing a P-wave tomographic velocity model; (c) inferring a local stress tensor for the site with focal mechanisms. In this study, we present our seismic and stress analysis results that advance the characterization of material properties, distribution of seismically active faults/fractures, and stress state in the reservoir. In the following sections, we first briefly introduce the geologic setting and operation history at San Emidio, the 2016 seismic data set, and the methodology of our analysis, and then present and discuss our results.

2. Basic Background of the San Emidio Geothermal Field

The San Emidio geothermal field is located in the southeastern part of the San Emidio Desert, which is located within the East-West extensional Basin and Range Province of northwestern Nevada, ~100 km north of Reno. It hosts a hidden, forced-convection geothermal system (Rhodes, 2011; Rhodes et al., 2011). It is located near the southernmost expression of the San Emidio Fault (SEF), a north-striking, west-dipping Holocene scarp hosting zones of intense hydrothermal alteration, surrounded by many closely spaced minor faults (Figure 1) (Folsom et al., 2020; Rhodes, 2011; Rhodes et al., 2011). The geologic cross-section shows that the deeper and hotter part of the reservoir consists of low-porosity Mesozoic metasedimentary and metavolcanic rocks, which are overlain by tertiary volcanic and sedimentary rocks at shallower depths (Rhodes, 2011; Rhodes et al., 2011). Due to the low permeability in the deeper and hotter reservoir, fluid transport is concentrated in the permeable fault zones (Folsom et al., 2020).

Production started in 1987 from shallow depths (~30–90 m below surface). Following the cooling of the shallow reservoir, deeper production wells were drilled to the north along the SEF and the initial, shallow production wells were converted to injection wells. More details about the field history are introduced by Folsom et al. (2020). The production is primarily from fractures hosted by mechanically strong, silicified tuff and lavas at depths of ~520–700 m below surface at temperatures of ~162°C, which are overlain by mechanically weak, clay-altered volcanoclastic rocks (Warren et al., 2018).

Several geophysical surveys have been performed in the field to investigate the subsurface structure (e.g., Folsom et al., 2020; Warren et al., 2018). Warren et al. (2018) mapped geothermal permeability using a passive seismic emission tomography method. Folsom et al. (2020) performed a 3-D inversion of magnetotelluric (MT) data. They also forward-modeled gravity data informed by geology, drilling, MT, and other results. Their results helped them to construct a conceptual block model of the subsurface including the 3-D distribution of fault surfaces and inferred stratigraphic contacts.

3. 2016 December Plant Shutdown and Seismic Data Set

From 2016-12-08 19:33 to 2016-12-09 15:00 UTC, the San Emidio power plant was shut down for 19.45 hr for maintenance (dark gray shading in Figure 2a). There are three vertical production wells and three vertical injection wells (red and blue triangles in Figure 1), which all stopped operating during the shutdown, except for a short resumption (Figure 2b).

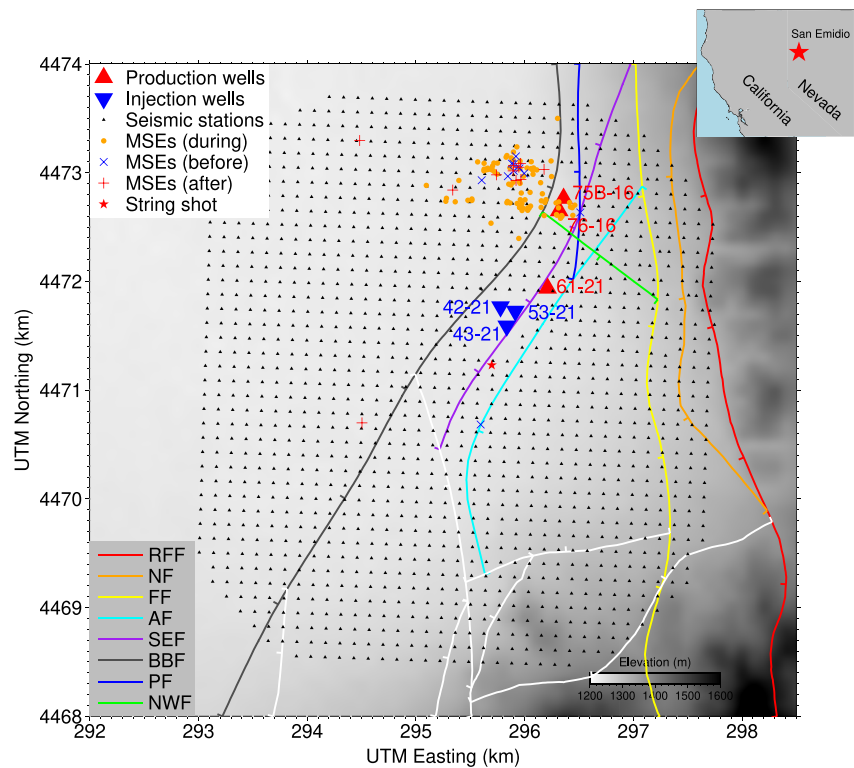


Figure 1. Map view of microseismicity and seismic station deployment in December 2016 at San Emidio. Blue crosses, orange dots, and red pluses represent catalog microseismic events (MSEs) before shutdown, during shutdown, and after restart, respectively. The Easting and Westing coordinates are in the Universal Transverse Mercator (UTM) coordinate system (zone 11 T). Black dots, seismic stations; red dot, string shot event; lines, fault traces at surface. Red and blue triangles represent active production and injection wells in 2016, respectively. The background gray image shows topography. RFF, Range front Fault; NF, Nightingale Fault; FF, Fan Fault; AF, Antithetic Fault; SEF, San Emidio Fault; BBF, Basin Bounding Fault; PF, Piedmont Fault; NWF, NW Fault. All the other faults in the southern part are shown as white lines. Tick marks on fault traces represent dip directions. The fault model has been updated from Folsom et al. (2020). The insert map on the top right shows the geographic location of San Emidio (red star).

A dense passive seismic array with 1,302 vertical-component seismographs, spaced approximately 80 m apart, was deployed at San Emidio during 5–11 December 2016 (Figure 1) (Lord et al., 2016a, 2016b; Warren et al., 2018). The primary aim was to advance the characterization of permeability using passive seismic emission tomography (PSET), a back-projection type technique (Sicking et al., 2012; Warren et al., 2018). In addition, 123 MSEs were detected, most of which were located within the northeastern part of the seismic array (Figure 1) (Warren et al., 2018). In addition to the MSEs, one string shot on 8 December 2016 was also recorded by the seismic array (Figure 1).

We cut event waveforms for the MSEs in the catalog of Warren et al. (2018) and the string shot. The waveforms were then processed by removing the mean and trend. We then performed bandpass filtering between 5 and 50 Hz based on the visual inspection of signal-to-noise ratio (SNR) from the spectra of several events. We picked P-wave arrivals for the catalog events and the string shot using an automatic arrival picking code (Guo et al., 2018), which is based on Akaike Information Criteria (Maeda, 1985). Figure S1 in Supporting Information S1 shows example waveforms and our P-wave arrival picks for one event. The arrivals were picked within preset time windows, which are 0.6 s before and 0.6 s after the theoretical arrival times calculated with the catalog locations and an existing velocity model from Warren et al. (2018). For each arrival pick, we scored its quality based on the SNR (the ratio of the root-mean-square amplitudes of the phase and noise windows). After picking arrivals, we removed the MSEs that had few or bad picks or had picks with large azimuth gaps, leaving 110 MSEs and one string shot to be used for the following analyses. S-wave signals are generally weak on vertical-component seismograms and therefore were not analyzed.

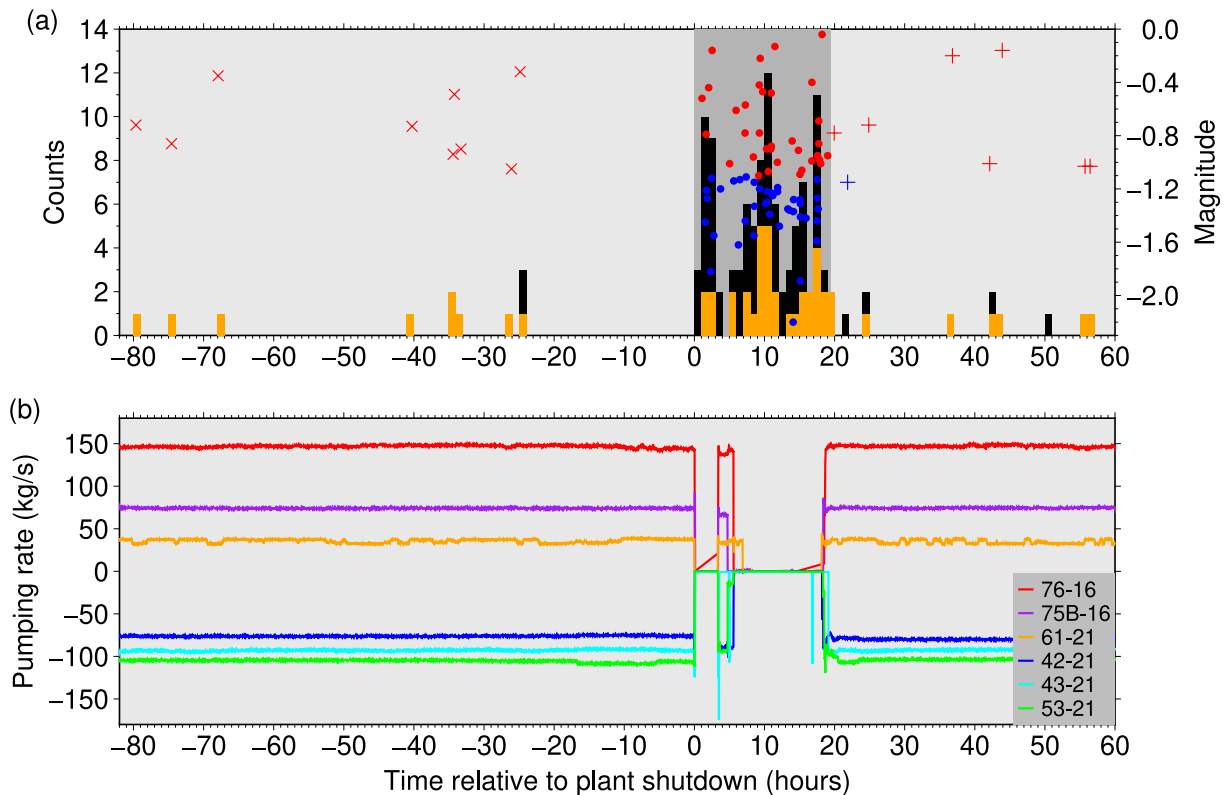


Figure 2. Temporal evolution of seismicity and pumping rates of production and injection. (a) Seismicity. The plant shutdown period ($t = 0$ – 19.45 hr) is shaded. The plant shutdown began at 2016-12-08 19:33 UTC. The number of MSEs per hour is shown as black and orange bars with the vertical axis shown on the left. The black bars are for all the events in the catalog. The orange bars are for the relocated events above magnitude -1.1 . Note that some black bars are completely covered by orange bars. Crosses, dots, and pluses show magnitudes (vertical axis on the right) of the relocated events before shutdown, during shutdown, and after restart, respectively. These symbols are colored in red and blue for the events above and below magnitude -1.1 , respectively. (b) Pumping rate (positive, production; negative, injection). The red, purple, and orange lines show the pumping rate evolution for the three production wells. The blue, cyan, and green lines are for the three injection wells. There is no pumping at all the wells during shutdown except for a short resumption within the 3–6 hr time window.

4. Methods and Results

4.1. Coda Duration Magnitude

To estimate the magnitudes of the seismic events, we calculated the coda duration magnitude (M_c), a common approach for small seismic events (e.g., Herrmann, 1975; Lee et al., 1972). We followed the approach used by the University of Utah Seismograph Stations (Koper et al., 2020; Pechmann et al., 2006). We first took the envelope for each successfully picked waveform. The logarithm of the waveform envelope was used for coda windowing, starting near the maximum amplitude after the theoretical S-wave arrival and ending at twice the pre-P noise level. We then linearly fit the windowed coda and defined the duration as the time of the end of coda when the best-fit line fell below a fixed cutoff value minus P-wave arrival time. Defining coda duration relative to a fixed cutoff value, instead of relative to the pre-P noise level, can mitigate the influence of temporal variations in ambient seismic noise (Koper et al., 2020), for example, day versus night and during shutdown versus before and after shutdown. The fixed cutoff value we used is the median value of the pre-event noise levels during shutdown (Figure S2 in Supporting Information S1), which were calculated as the mean of the log10 envelope of the noise window within 1 s before P-wave arrival on each station for each event. The station M_c was then calculated based on the empirical M_c -duration τ formula:

$$M_c = 2.65 \log_{10}(\tau) - 1.7, \quad (1)$$

which is used by the Nevada Seismological Laboratory for the Nevada region. The final event magnitude was defined by taking the median of the M_c values from at least three stations. We successfully calculated magnitudes for 91 of our relocated events, which are all very small ranging from -2.2 to 0 , as shown in Figures 2a, 3a, and 3b.

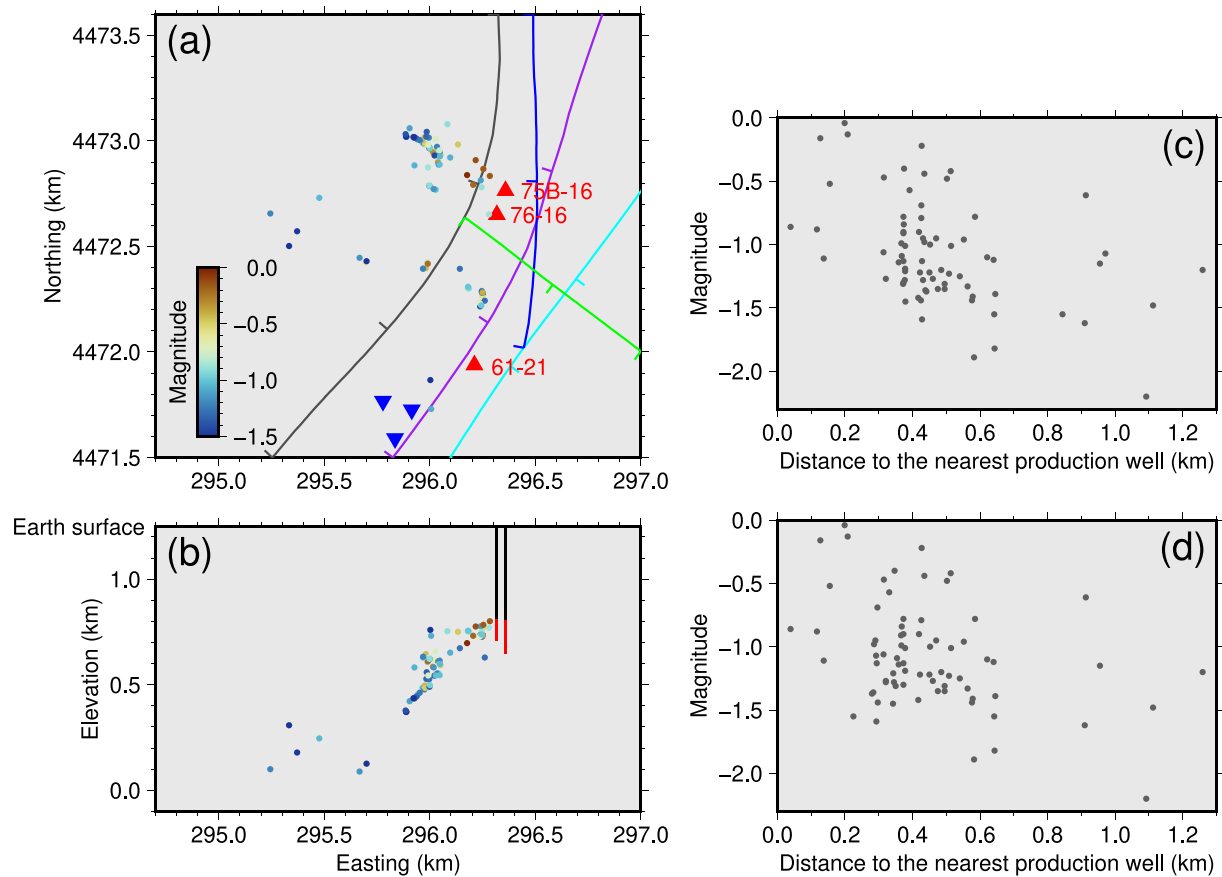


Figure 3. Event magnitude. (a) Map view and (b) cross-section of event magnitudes. 91 of our relocated events with magnitude estimates are shown as dots colored by magnitudes. Red and blue triangles, production and injection wells, respectively; Lines, fault traces at the surface (gray: BBF; purple: SEF; blue: PF; green: NWF; cyan: AF). Note all the wells are vertical. On the cross-section, the two vertical lines are the depth trajectories of production wells 75B-16 and 76-16, and the red segments of the lines are the perforated sections. (c) Magnitude versus the distance from hypocenter to the middle of the perforated section of the nearest production well (75B-16 or 76-16) for the events during shutdown. (d) Same as (c) except that the southern production well 61-21 is also used for calculating distances.

4.2. Triple-Difference Seismic Location and Tomography

We relocated catalog events and determined a 3-D model of P-wave velocity (V_p) using the triple-difference seismic location and tomography algorithm *tomoTD* (Guo et al., 2021; Guo & Zhang, 2017). *tomoTD* is an arrival-time based tomography technique that was modified from the double-difference tomography algorithm *tomoDD* (Zhang & Thurber, 2003, 2006). *tomoTD* is able to combine absolute arrival times and station-pair, event-pair, and double-pair differential arrival times to invert for event locations and a 3-D velocity model simultaneously. The three types of differential time data have their respective advantages in determining event locations and velocity model (Guo et al., 2021; Guo & Zhang, 2017). The station-pair differential time data from an event to pairs of stations are more sensitive to absolute event locations and the velocity model beneath the stations. The event-pair differential time data from pairs of events at a station are more sensitive to relative event locations and the velocity model of the source region. The double-pair differential time data from pairs of events at pairs of stations have similar benefits as the event-pair data but can further remove the effect of origin time errors. *tomoTD* solves a linearized inversion system, which is stabilized by damping and smoothing constraints.

We constructed event-pair, station-pair, and double-pair catalog differential time data from our picked absolute arrival times (note that our picked arrival time data are called catalog data). Constructing event-pair and double-pair catalog differential time data relies on relative locations between events. Since the relative event locations are not well constrained in the original catalog, we first conducted a preliminary inversion to improve the event locations and then used the event relocations to reconstruct the differential time data. We also measured P-wave waveform cross-correlation (WCC) differential times from pairs of events separated by 1 km or less, following the time-domain WCC method of Schaff et al. (2004). The measurements with WCC coefficients below 0.7 were

discarded. The event-pair WCC differential time data were used to construct the double-pair WCC differential time data. In total, our final input P-wave data set includes 34,008 absolute arrivals, 1,092,974 station-pair catalog differential times, 247,856 event-pair catalog differential times, 554,912 double-pair catalog differential times, 103,847 event-pair WCC differential times, and 382,107 double-pair WCC differential times.

Our tomographic inversion uses the Universal Transverse Mercator (UTM) coordinate system and has a velocity model grid spacing of ~ 0.2 – 0.3 km in the Easting, Northing, and vertical directions in the regions with event and station coverage (Figure S3 in Supporting Information S1). We started from the catalog event locations and the Vp model from Warren et al. (2018) (Figures S4 and S5 in Supporting Information S1). As mentioned in Section 3, the catalog events were detected and located using PSET, a beamforming type technique (Warren et al., 2018). The Vp model of Warren et al. (2018) was guided by one seismic imaging profile along an active-source line at a Northing of ~ 4471.7 km and modified to fit the arrivals of downhole string shot data.

We selected the optimal smoothing by testing a range of smoothing values and chose the one that balanced the model smoothness and data residual reduction. We selected the damping value to constrain the condition number of the inversion within a reasonable range of around 100–200. After the inversion, the root-mean-square (RMS) data residual decreased from 0.128 to 0.079 s for the catalog data and from 0.096 to 0.031 s for the WCC dt data. We performed bootstrap analysis, a statistical method (Efron & Gong, 1983; Efron & Tibshirani, 1991; Waldhauser and Ellsworth, 2000), to estimate event location uncertainties following Guo and Zhang (2017) (Text S1 in Supporting Information S1). To assess model resolution, we conducted noise-free and noise-added checkerboard tests with varying checkerboard sizes and used the method of Zelt (1998) to quantitatively calculate checkerboard model resolvability (Text S2 in Supporting Information S1). Figures S6–S9 in Supporting Information S1 show that at shallow depths (above 0.8 km elevation), the model is well resolved in the northern and central parts of the study area, whereas at greater depths (below 0.8 km elevation) only the seismically active region in the northeastern part is well resolved.

After the inversion, 106 of 110 events were relocated successfully. Figure 4b shows the horizontal and cross-section views of our relocations, which are much more concentrated compared to the catalog locations shown in Figure 4a. Most events are within 600 m to the northwest of the two northern production wells. On the E-W cross-section, event relocations generally dip to the west and the majority are between 0.4 and 0.85 km elevation. The main seismicity cluster at ~ 296 km Easting, $\sim 4,473$ km Northing, and ~ 0.4 – 0.6 km elevation forms a westward dipping lineation with $\sim 60^\circ$ dip angle, which we consider to be reliable given the small location uncertainty estimates as shown in Figure 4b. There are only 2 events located near the injection wells.

Figures 5 and 6 and Figure S10 in Supporting Information S1 show the depth slices and cross-section of our new Vp model. Note that in Figures 5 and 6c and Figure S10c in Supporting Information S1 we show the Vp model perturbation in percentage relative to the 1D model calculated by averaging velocities at each depth. The well-resolved parts of the model as estimated by the resolution tests are outlined. It is noteworthy that the initial model embodies some large-scale structure features, including the velocity contrast on the two sides of the Range Front Fault at an Easting of ~ 297.5 km and the stair-step structure going from east to west (Figures S4 and S5 in Supporting Information S1). Compared to the initial model, our new model refines the shallow structure beneath the seismic array and the structure of the seismically active parts of the reservoir (Figures 5 and 6b; Figure S10 in Supporting Information S1), as suggested by the resolution tests (Figures S6–S9 in Supporting Information S1). The velocity contrast characterizing the range front at an Easting of ~ 297 km becomes sharper and more continuous from north to south (Figure 5).

The SEF, Piedmont Fault (PF), and Basin Bounding Fault (BBF), along which the geothermal reservoir is developed, are associated with low-velocity anomalies at 0.3–0.8 km elevation (Figures 6b and 6c; Figure S10 in Supporting Information S1). The SEF and PF are delineated by a strong velocity contrast from high velocity on their eastern side to low velocity on their western side (Figure 6b). To the west of the PF and SEF, there is a zone from ~ 1.8 to ~ 3.3 km distance along profile AA' at 0.3–0.8 km elevation, as outlined in Figure 6c, with negative velocity perturbations as low as -25% , much lower than the zone just above. The BBF cuts through this extremely low-velocity zone. It is also located to the west of the production wells 75B-16 and 76-16 (note the perforated sections of the wells are in contact with PF and SEF) (Figures 6b and 6c). All the events to the northwest of wells 75B-16 and 76-16 occurred on the BBF and in the area between the PF and BBF, which are contained within this low-velocity zone (Figures 6a–6c). The other MSEs are distributed in the low-velocity zone bounded and/or crossed by the BBF, SEF, PF, and NW Fault (NWF) and tapped by the nearby production wells (Figure S10

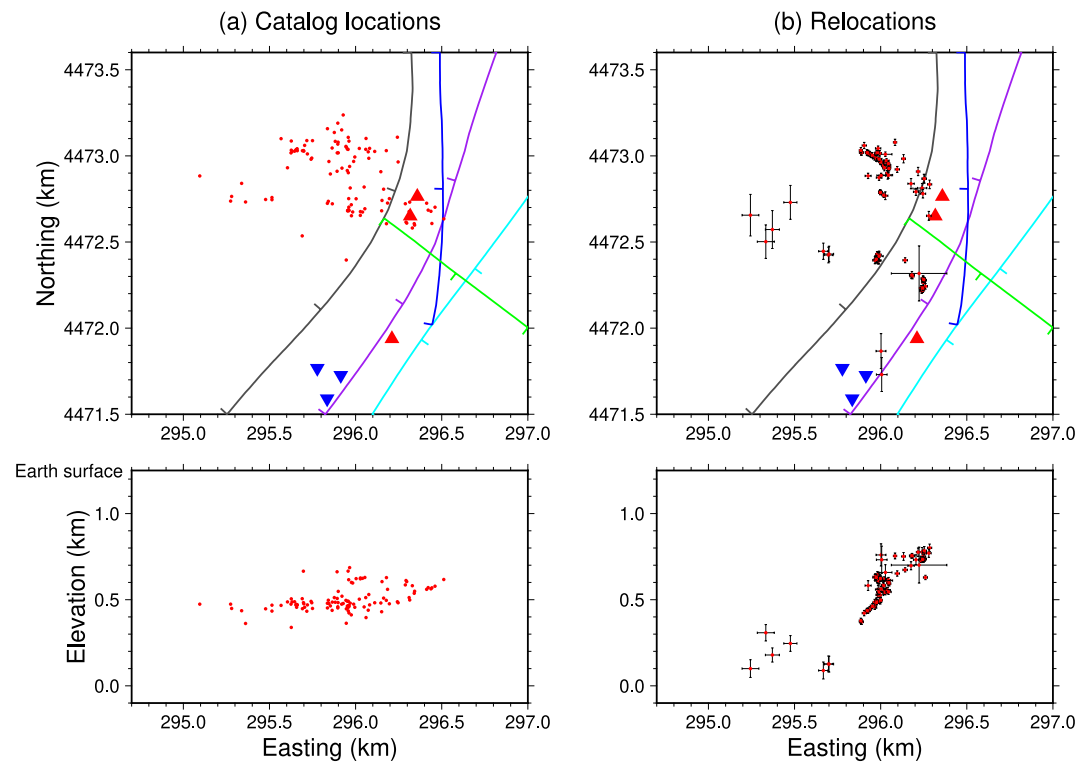


Figure 4. Comparison of (a) catalog event locations and (b) our relocations in map view and cross-section. Lines, fault traces at the surface (gray: BBF; purple: SEF; blue: PF; green: NWF; cyan: AF); red and blue triangles, production and injection wells, respectively. In (b), the error bars represent the event location uncertainty estimates using bootstrap analysis.

in Supporting Information S1), except for a few deeper events (Figures 6b and 6c; Figure S10 in Supporting Information S1).

Figure 7 zooms in our MSE relocations and V_p model in the region where the main seismicity cluster and all the MSEs before plant shutdown and after plant restart occurred. Most MSEs before shutdown and after restart occurred in a very localized zone at the top of the main seismicity cluster, which is associated with the lowest velocity values (2.8–3.0 km/s).

4.3. Focal Mechanism Inversion

We computed first-motion focal mechanisms for catalog MSEs using the HASH algorithm (Hardebeck & Shearer, 2002). P-wave first-motion polarities were automatically identified for our arrival picks using a method similar to Chen and Holland (2016), which is designed to simulate how an analyst determines the phase polarity by comparing the phase amplitude to the pre-phase noise level. This was done by first searching for a local maximum or minimum after the arrival pick and then calculating the ratio between the amplitude of the pick and pre-pick noise amplitude, that is, the signal-to-noise ratio (SNR). The SNR values were then used to decide which polarity picks to be used. Example polarity picks and the corresponding SNR values are shown in Figure S1 in Supporting Information S1. In general, higher SNR thresholds eliminate more wrong polarity picks at the cost of losing more correct polarity picks, whereas smaller SNR thresholds provide more polarities but include more incorrect decisions. After testing a set of SNR thresholds, we set the threshold value to $\text{SNR} = 5$. This value yields the most high-quality focal mechanisms while providing relatively small fault plane uncertainties.

HASH searches for a set of acceptable focal mechanisms for each event while accounting for possible errors in earthquake locations, velocity model, and polarity observations. We input azimuth and takeoff angle for each event-station pair computed with our final event relocations and 3-D V_p model. For each event, the average of the set of acceptable mechanisms is the preferred mechanism and the uncertainty is calculated based on the distribution of acceptable mechanisms. Kilb and Hardebeck (2006) found that the average of the fault plane uncertainty

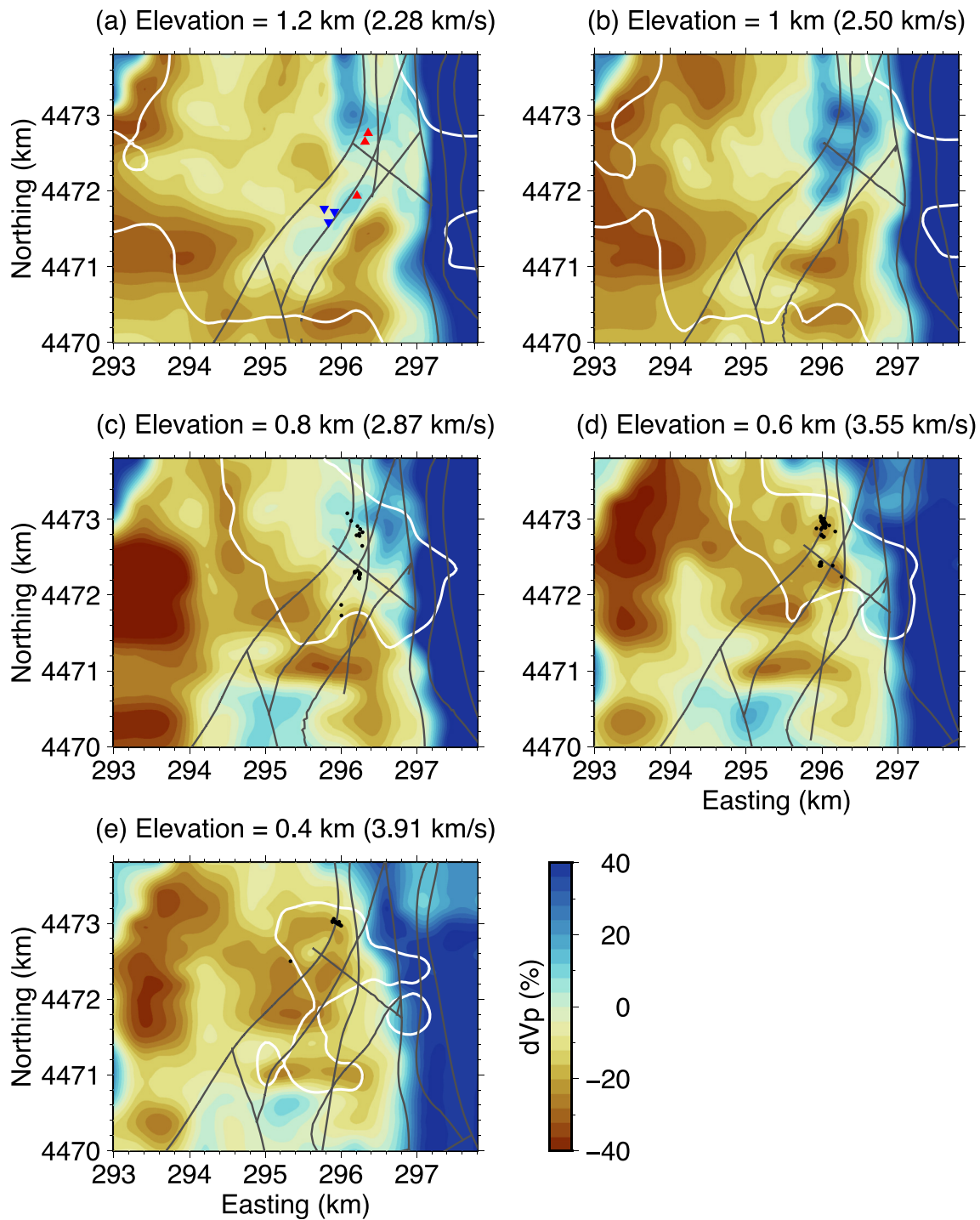


Figure 5. Depth slices of the inverted V_p model. Each panel shows the V_p model perturbation in percentage relative to the 1-D depth-averaged model at each depth. The depth-averaged V_p value at each depth is given in the title. Black dots represent the MSEs within 0.1 km of each slice. Gray lines represent the fault traces at each depth (fault model updated from Folsom et al., 2020). The red and blue triangles in (a) represent production and injection wells, respectively. The white lines represent the model resolvability contour of 0.7, estimated from the 3-by-3-by-3 checkerboard resolution test (Figures S6 in Supporting Information S1), outlining the well-resolved regions.

and auxiliary plane uncertainty was the best indicator of mechanism quality, with values less than 35° indicating the best mechanisms. We defined quality A and B mechanisms such that the average fault plane uncertainty is less than 25° and 35° , respectively.

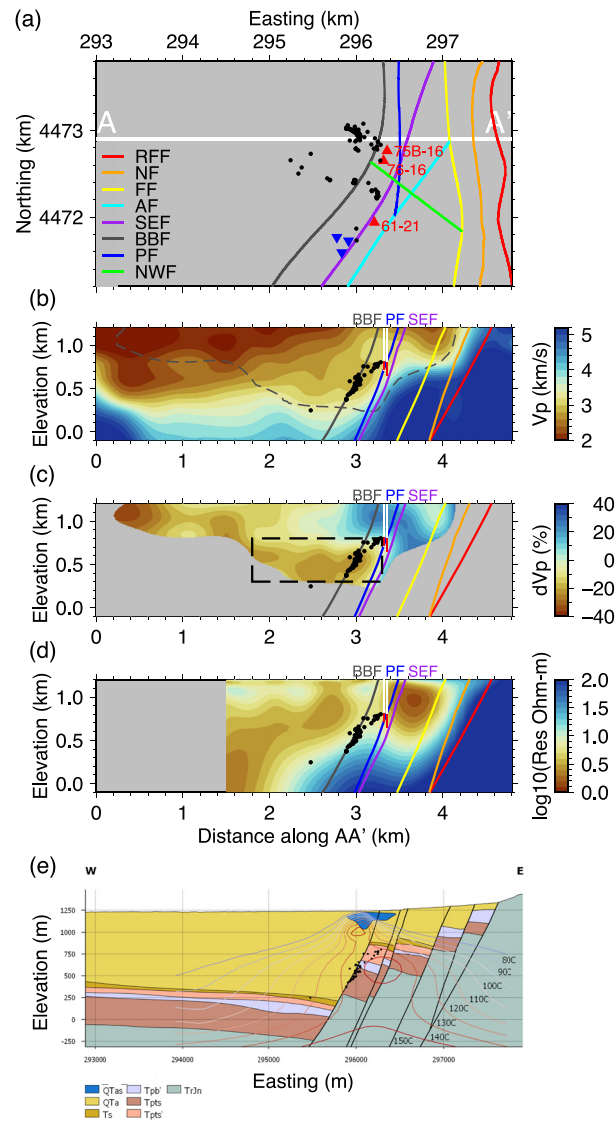


Figure 6. Cross-sections of the MSE relocations, Vp model, resistivity model, temperature model, geology model, and well trajectories along profile AA' shown in (a). (a) Map view of MSE relocations (dots) and fault trace at the surface (colored lines), and production (red triangles) and injection (blue triangles) wells. Note that all the wells are vertical. The white line shows the profile AA'. (b) Vp model. The depth trajectories of wells 75B-16 and 76-16 (white-to-red lines with the red segments representing the perforated sections) and fault traces at depth (colored dipping lines) are projected. The dashed gray lines represent the model resolvability contour of 0.7, estimated from the 3-by-3-by-3 checkerboard resolution test (Figure S6 in Supporting Information S1), outlining the well-resolved region (but note the small gray circle is likely an artifact of the resolvability estimation). (c) Vp model perturbation in percentage relative to the 1-D depth-averaged model. The low-resolution regions are masked. (d) Resistivity model from Folsom et al. (2020). The region where there is no MT station at the surface is cut. (e) Geologic and temperature models. Iso-temperature curves (80–150°C) are shown. QTas, silicified sediments; QTa, Alluvium is further subdivided by grain size and clay content; Ts, Late Miocene siltstones, tilted and indurated; Tpb', Upper basaltic andesite; Tpts, Lower tuffs; Tpts', Upper tuffs and tuffaceous sediments; TrJn, Nightingale. The temperature model is from Folsom et al. (2020). The geologic model has been updated from Rhodes (2011) and Folsom et al. (2020). In (b–e), the MSEs within 0.2 km of the cross-section are shown as black dots.

One concern regarding focal mechanism inversion is whether the station polarities sample the focal sphere well, depending on the event depth and station distribution. In Figure S11 in Supporting Information S1, we show polarities on the focal sphere for three example events in different clusters. In general, the polarities are well distributed on the focal sphere for the high-quality mechanisms. Owing to the wide distribution of stations compared to the very shallow depths of events, P waves recorded on the stations near event epicenters leave sources in the upward

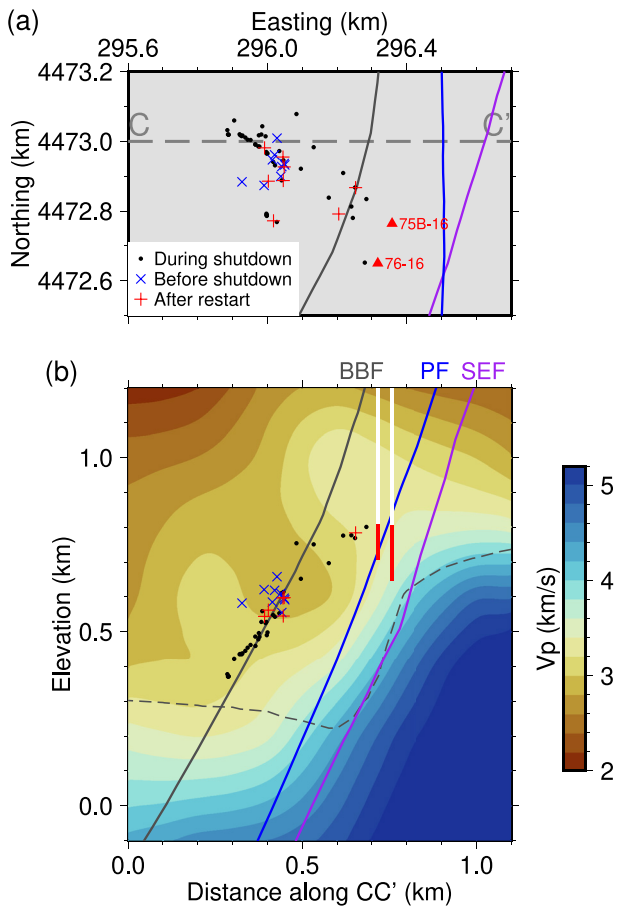


Figure 7. Cross-section of MSEs and the V_p model enlarged around the main cluster of seismicity. (a) Map view of MSE relocations (crosses, before shutdown; dots, during shutdown; pluses, after restart) and fault trace at the surface (gray line, BBF; blue line, PF; purple line, SEF), and production wells (red triangles). (b) The V_p model cross-section along profile CC' shown in (a). The depth trajectories of the two production wells (white-to-red lines with the red segments representing the perforated sections) and fault traces at depth (colored dipping lines) are projected. The dashed gray line outlines the well-resolved region.

direction whereas for the ones recorded on the stations far from the event epicenters they leave sources downward. Thus, the upgoing and down-going ray paths sample the focal spheres well (Figure S11 in Supporting Information S1). Most of the polarities are located in the expected quadrants although there are some misfits. The misfits are likely due to a combination of error sources: (a) incorrect polarity picks; (b) the assumption of pure double couple mechanism, which may not be appropriate for all the events; and (c) errors in the inverted focal mechanisms. We tried higher SNR thresholds to exclude more wrong polarity data at the cost of losing more correct data but the inverted focal mechanisms are not significantly changed.

Figures 8a and 8b show our high-quality focal mechanism results for 36 events (3 quality A and 33 quality B), from which we identified two clusters (C1 and C2) with at least 10 mechanisms. Most events are dominated by normal slip but also show strike-slip components except for the events in C2, many of which are dominated by strike slip (Figure 8b). No event is dominated by reverse slip. The fault/fracture orientations seen from the focal mechanisms have a large variability, but appear more similar among each individual cluster, especially C1 and C2. Figures 8c–8e enlarge C1 and C2. The events in C1 are dominated by normal slip with strike and dip angles generally consistent with the seismicity lineation (Figures 8c and 8d). The events in C2 form an elongated zone striking NNE and one of the nodal planes for each strike-slip event is generally aligned in a similar direction (Figure 8e).

4.4. Stress Inversion

We estimated the stress-field orientation from the MSE focal mechanisms using the MSATSI algorithm (Martínez-Garzón, Kwiatek, Ickrath, & Bohnhoff, 2014), which is a MATLAB software package redesigned from the SATSI algorithm (Hardebeck & Michael, 2006). MSATSI is a robust, linearized method that uses damped least-squares optimization to invert for the orientations of the principal axes of stress and the ratio R of their relative magnitude:

$$R = \frac{\sigma_1 - \sigma_2}{\sigma_1 - \sigma_3}, \quad (2)$$

where σ_1 , σ_2 , and σ_3 represent the maximum, intermediate, and minimum principal stresses, respectively. The bootstrap resampling method is applied to the input focal mechanism data for estimating uncertainties. Figure 9

shows the stress inversion results, including the final stress tensors (Figures 9b, 9d, and 9f) and 1,000 bootstrap solutions (Figures 9a, 9c, and 9e), using all high-quality (quality A and B) focal mechanisms (Figures 9a and 9b) and the mechanisms in C1 (Figures 9c and 9d) and C2 (Figures 9e and 9f) only. The other clusters are not analyzed separately due to their limited mechanisms available.

The entire northeastern part of the seismic array where the focal mechanisms are located (Figure 8a) shows a normal faulting dominated stress regime (Figure 9b). The fairly concentrated solutions from the bootstrap inversions for each principal stress direction indicate the robustness of the final solution (Figure 9a). The stress tensor is generally aligned with the geometry of the normal faults SEF, BBF, and PF in the northeastern part of the seismic array (Figures 8a, 9a, and 9b): σ_1 is essentially vertical, σ_2 is close to horizontal and trends north-south, parallel to the strike of those faults, and σ_3 is close to horizontal and trends east-west, normal to the strike of those faults. The R value is 0.44. As noted by Jahnke et al. (2023), this overall reservoir stress state is consistent with other stress indicators, including the World Stress Map (Heidbach et al., 2018), slickenlines, wellbore stress indicators from nearby geothermal fields, and secular strain rate measurements.

However, the local stress states in C1 and C2 are markedly different (Figures 9c–9f), indicating stress heterogeneity in the reservoir. C1 has a normal faulting environment with σ_1 close to vertical, σ_2 close to horizontal and

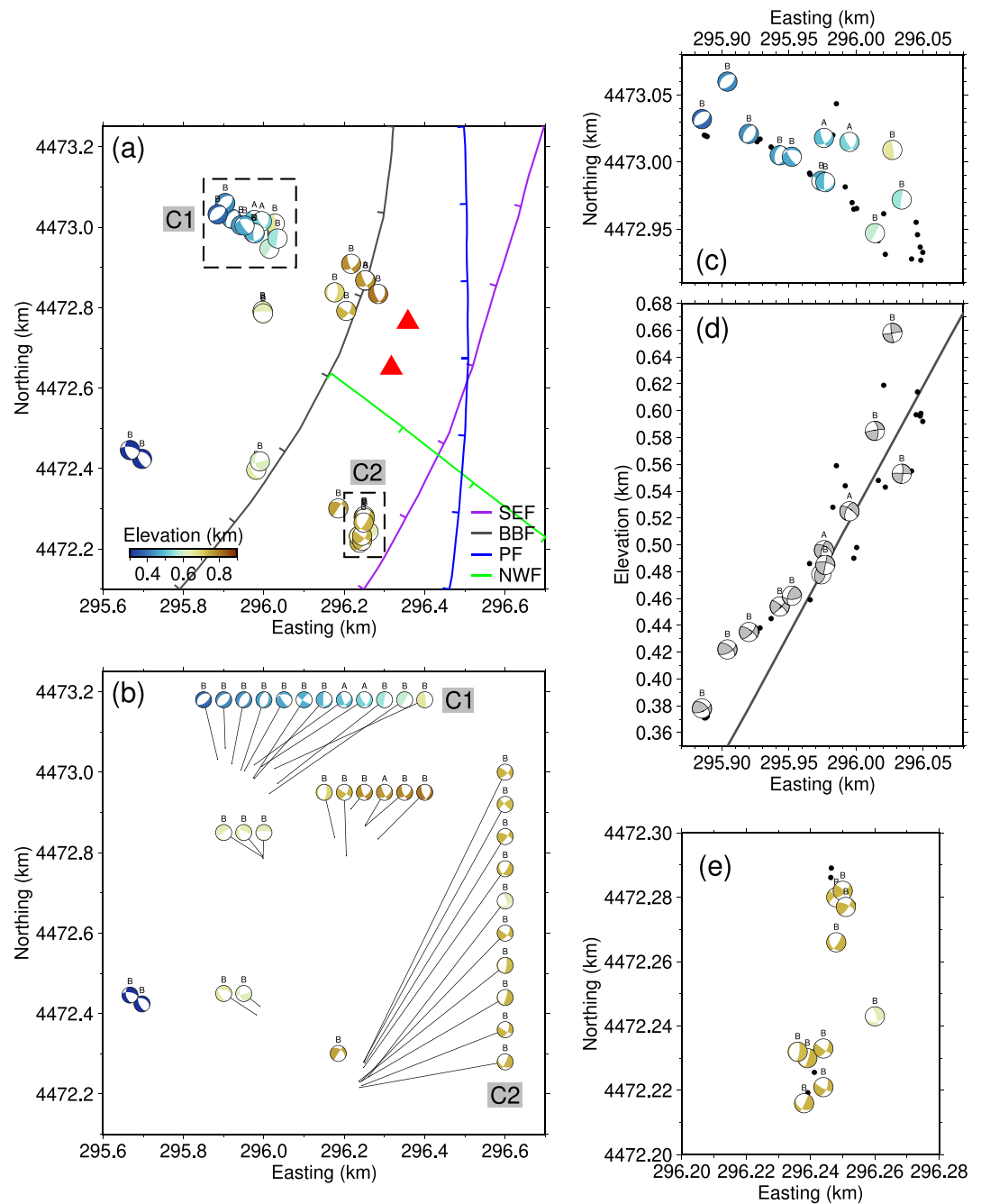


Figure 8. MSE focal mechanisms. (a) Map view of all the inverted focal mechanisms (lower hemisphere beach balls). Dashed rectangles outline the two clusters C1 and C2 that are zoomed in (c) and (e). (b) The same focal mechanisms as in (a). All the mechanisms are plotted separately from each other and connected with event epicenters. (c, d) Zoom-in map view and cross-section of C1. Note that in (d) the mechanisms are rotated to the E-W cross-section view. (e) Zoomed-in map view of C2. Black dots in (c–e) show the events that do not have focal mechanism results. The focal mechanism quality (A or B) is labeled above each beach ball.

trending SSW, and σ_3 close to horizontal and trending WNW (Figure 9d). Given this stress state, the ideal orientation of the failure plane is the one striking to NNE and dipping $\sim 60^\circ$, consistent with the geometry of the BBF and the seismicity observations (Figures 8a, 8c, and 8d). C2 has a trans-tensional stress regime dominated by strike slip with a normal slip component (Figure 9f), consistent with the resolved focal mechanisms (Figures 8b and 8e). The R values for C1 and C2 are 0.62 and 0.45, respectively.

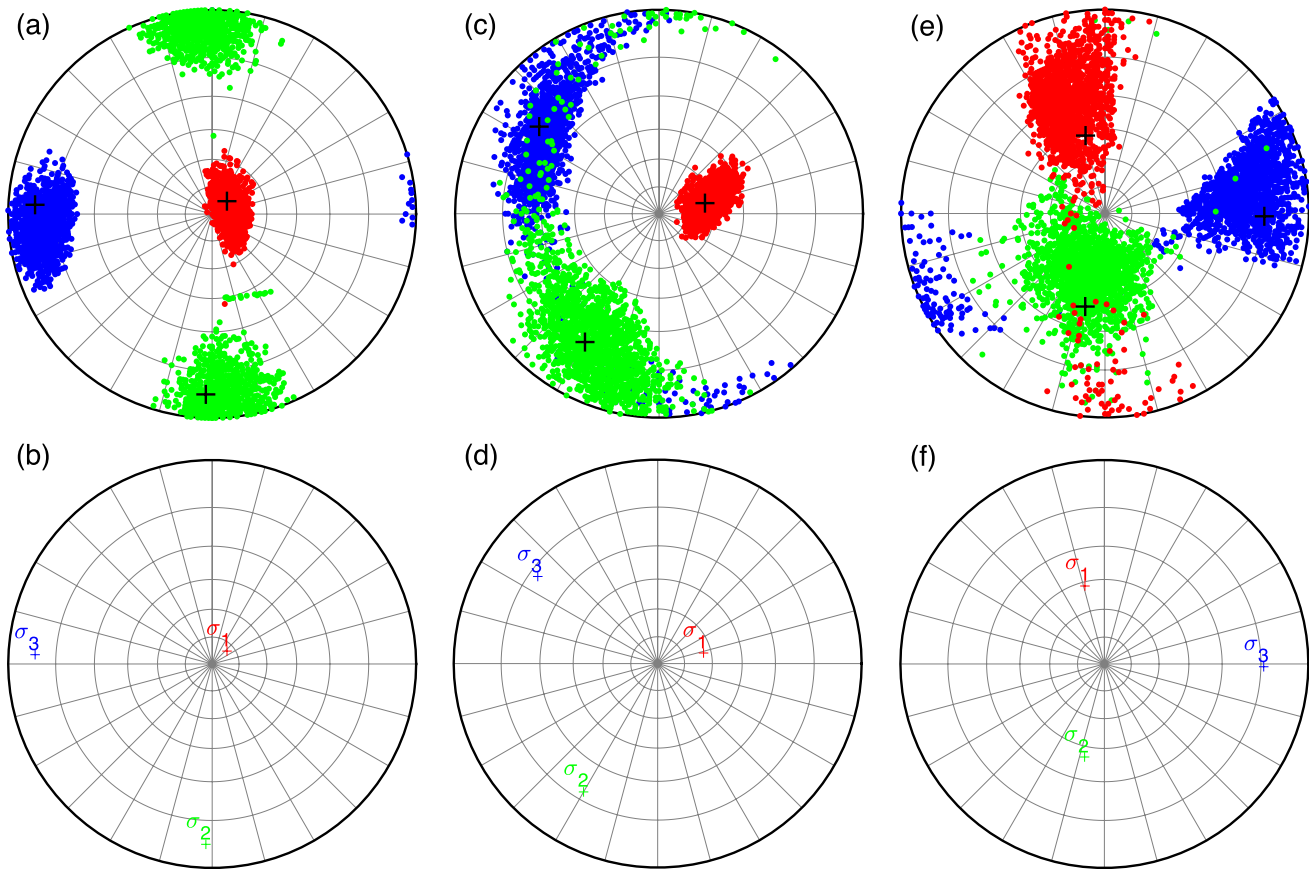


Figure 9. Stress inversion results. (a, c, e) 1000 bootstrap solutions (dots) and (b, d, f) the best solution (pluses) using high-quality focal mechanisms (a, b) in the whole study area and in the clusters (c, d) C1 and (e, f) C2 only. In the top panels, red, green, and blue dots represent the maximum (σ_1), intermediate (σ_2), and minimum (σ_3) principal stresses, respectively; black pluses represent the best solution, the same as that shown in the bottom panels. The relative stress magnitude R values for (b, d, and f) are 0.44, 0.62, and 0.45, respectively.

Using a preliminary set of our focal mechanisms determined with preliminary event locations and a 1-D velocity model, Jahnke et al. (2023) conducted stress inversions using the method of Vavryčuk (2014) and calculated slip tendency for each inferred fault plane given a set of potential initial stress models. In general, we have better constraints on the stress tensor orientation and relative stress magnitude due to more and higher-quality focal mechanisms available owing to more accurate predictions of azimuth and take-off angle for each event-station pair with the finalized event locations and 3-D velocity model.

5. Discussion

In this section, we first discuss the effect of varying noise on detected seismicity during different periods, reservoir material properties, and the distribution of seismically active faults/fractures and then discuss the mechanism for inducing MSEs during plant shutdown.

5.1. The Effect of Varying Noise on Detected Seismicity Before, During, and After Shutdown

The catalog of Warren et al. (2018) shows enhanced seismicity during plant shutdown (Figure 2a). However, changes in the rate of the detected seismicity may be caused by the varying ambient noise during different periods. We compared the pre-event noise levels before, during, and after shutdown (see Section 4.1 for how we calculated the pre-event noise) and the result shows that the noise level is lower during shutdown (Figure S2 in Supporting Information S1). As shown in Figure 2a, almost all of the smaller events below magnitude -1.1 were detected during shutdown (blue dots), which is likely due to the lower noise level. Above magnitude -1.1 ,

the detection capability is likely comparable during all periods. There are 9 events of magnitude -1.1 and above during the 80 hr before shutdown (0.11 events per hour), 34 during the 19.45 hr of shutdown (1.75 events per hour), and 7 events in the 40 hr after restart (0.18 events per hour) (Figure 2a). This indicates the enhanced microseismicity during shutdown is a reliable observation.

5.2. Reservoir Material Properties and Distribution of Faults and Fractures

The broad distribution of seismicity clusters in the map view and the very small event magnitudes suggest that the MSEs in different clusters happened on small, isolated fault patches and fractures (Figures 3–7). MSE relocations and focal mechanisms suggest that the main cluster C1 to the northwest of the production wells 75B-16 and 76-16 occurred on a small patch of the BBF at an elevation of 0.4–0.7 km (Figures 6a, 6b, 7, 8c, and 8d). This cluster forms a linear structure on the fault surface, striking to the northwest, as seen from the horizontal and cross-section views (Figures 6a, 6b, and 7). Such microseismic lineations, that is, streaks, aligned in the slip direction have been observed in tectonic fault zones and are interpreted to be structural or compositional in origin (e.g., Rubin et al., 1999; Waldhauser et al., 2004). The seismicity lineation and the nodal planes of the strike-slip mechanisms in cluster C2 suggest a previously unmapped strike-slip fault, striking approximately NNE (Figure 8e). The other MSEs between the BBF, PF, SEF, and NWF probably occurred on small-scale fractures within the damage zones associated with the individual faults (Figures 6a, 6b, 8a, and 8b; Figure S10 in Supporting Information S1).

Our V_p model and event relocations show that the BBF and the area between the BBF, PF, SEF, and NWF, where most MSEs occurred, are within a low-velocity body with a length of ~ 1 km at 0.3–0.8 km elevation (Figure 6c; Figure S10 in Supporting Information S1). This zone has negative velocity perturbation values as low as -25% , much lower than that in the zone just above, which indicates that the extremely low-velocity values in this zone are not due only to varying lithology from west to east (Figure 6e). In comparison, the overlying zone at 0.8–1.2 km elevation that has lower velocities compared to the eastern region (Figures 6b and 6c) may simply reflect a change in lithology from west to east.

According to theoretical and experimental studies, V_p is related to the bulk modulus, shear modulus, and bulk density of the rock, as well as its pore properties (e.g., Hutchings et al., 2019; Winkler & Nur, 1979). For a liquid-dominated geothermal reservoir, the main mechanism for decreasing its V_p is likely due to decreased bulk and shear modulus caused by increased rock damage (i.e., more cracks and fractures) and high fluid-filled porosity (e.g., Hutchings et al., 2019). The extremely low-velocity body is also characterized by high temperature and low resistivity (Folsom et al., 2020) and is in contact with the perforated sections of the nearby active production wells (Figure 6; Figure S10 in Supporting Information S1). Note that the production wells were perforated at these depths due to the geology (permeable fractures). The spatial coincidence of the high-temperature, low-velocity, low-resistivity zones with the fault patches and fractures delineated by the MSEs indicates this part of the geothermal reservoir around the production wells is fractured and presumably permeable such that fluids can flow through the BBF, PF, SEF, and NWF, and the fractures in between them. The stress regime at San Emidio is dominated by normal faulting (Figures 9a and 9b). However, local variations in fracture orientations and stress distribution can be expected for such a fractured, fluid-filled reservoir, as is evident by the diverse focal mechanisms with a wide range of orientations (Figure 8b) and the spatial variation in local stress state between different clusters (Figures 9c–9f).

5.3. Proposed Mechanism for Inducing MSEs Due To Production Pumping Cessation

During plant shutdown, most of the MSEs occurred on the BBF and the fractures between BBF, PF, and SEF near the perforated sections of the production wells (Figure 7; Figure S10 in Supporting Information S1). To explain a similar observation at the Brady Hot Springs geothermal field in Nevada, Cardiff et al. (2018) proposed that such enhanced microseismicity during a production cessation was caused by the pore pressure P_p recovery, decreasing effective normal stress and favoring MSEs. Pressure changes within the San Emidio reservoir were not monitored during the 2016 December shutdown. However, pumping tests performed in October 2016 with flow rate changes comparable to those during the December shutdown produced maximum measured pressure changes of 30 kPa (Cardiff et al., 2023b). The hydrologic modeling result also suggests P_p increases of the order of a few tens of kPa during the December shutdown around the production wells 75B-16 and 76-16 where most MSEs occurred (see

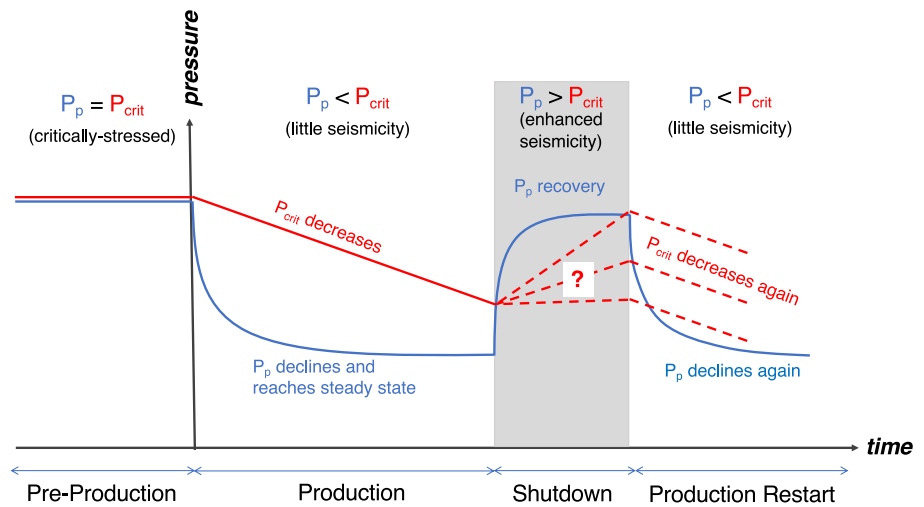


Figure 10. Schematic diagram of mechanism for inducing microseismicity during the production pumping cessation at San Emidio, which is described in terms of how the pore pressure P_p (blue curve) and critical pore pressure P_{crit} (red curve) evolve over time. The shutdown at San Emidio in December 2016 (gray shaded area) continued for 19.45 hr.

Figure 16 of Feigl et al. (2022)). Thus, both the hydrologic observations and modeling support the hypothesis that the MSEs during shutdown are a result of the P_p recovery due to the cessation of production pumping. However, the recovery of P_p provides only a necessary, not a sufficient, condition for rock failure and inducing MSEs. The reservoir must reach a critical stress state before shutdown so that P_p increases of the order of a few tens of kPa during shutdown could trigger fault slip.

Pumping at the injection wells also stopped during plant shutdown (Figures 1 and 2). The microseismicity is not likely to be caused by the cessation of injection pumping for two reasons. First, the MSEs observed during shutdown are much closer to the production wells than to the injection wells (Figure 4b). Second, the hydrologic modeling indicated P_p decreases around the injection wells during shutdown (see Figure 16 of Feigl et al. (2022)), which would inhibit fault slip.

We propose a conceptual model for the microseisms associated with the cycle of plant operations. As sketched in Figure 10, this model describes how the pore pressure P_p (blue curve) and critical pore pressure P_{crit} (red curve) evolve over time due to plant operations and reservoir stress changes. Critical pore pressure P_{crit} is the magnitude of pore pressure above which faulting is induced which depends on the reservoir stress state and frictional strengths of faults, commonly used in reservoir geomechanics (Zoback, 2007). Below we describe how P_{crit} is related to the reservoir stress state and fault strength.

First, we clarify the mechanical setting and underlying assumptions. As constrained by this study (Figure 9) and Jahnke et al. (2023), the faulting environment is either normal faulting ($S_v > S_{Hmax} > S_{Hmin}$) or trans-tensional ($S_v = S_{Hmax} > S_{Hmin}$), where S_v , S_{Hmax} , and S_{Hmin} are vertical, maximum horizontal, and minimum horizontal principal stresses, respectively. Thus, the maximum principal stress (σ_1) is either S_v or S_{Hmax} , and the minimum principal stress (σ_3) is always S_{Hmin} . S_{Hmax} will either stay constant or decrease due to reservoir cooling and local tectonics (secular strain rates from GPS show areal dilation at San Emidio according to Kreemer et al. (2012)), so we consider S_v to be σ_1 . If we consider failure on optimally oriented fault planes, which is the case for the normal faults in San Emidio, the relation between principal stress and pore pressure (P_p) magnitudes at failure can be described using the Coulomb criterion as:

$$S_v - P_p = (S_{Hmin} - P_p) \frac{1 + \sin\phi}{1 - \sin\phi} \quad (3)$$

where ϕ is the friction angle. From Equation 3, we can derive the expression for P_{crit} by solving for P_p ,

$$P_{crit} = \frac{1 + \sin\phi}{2 \sin\phi} S_{Hmin} - \frac{1 - \sin\phi}{2 \sin\phi} S_v \quad (4)$$

This equation provides the magnitude of P_p required to induce slip, given knowledge about the principal stress magnitudes. Because S_v does not change due to reservoir cooling or local tectonics considered here, P_{crit} is only influenced by the change in S_{hmin} (ΔS_{hmin}).

$$\Delta P_{crit} = \frac{1 + \sin\phi}{2\sin\phi} \Delta S_{hmin} \quad (5)$$

If we consider a friction angle of 30° , typical of crustal materials, Equation 5 shows that the change in P_{crit} (ΔP_{crit}) is a factor of 1.5 greater than ΔS_{hmin} .

Next, we discuss qualitatively how ΔS_{hmin} and ΔP_{crit} evolve over time during plant operation. A quantitative analysis requires cooling data and precise estimates of thermal expansion coefficient that are not currently available to us and is also out of the scope of this study.

Before the beginning of production, we assume that the crust is critically stressed such that P_p and P_{crit} are at the same level.

During normal operations, pumping at production wells decreases pore pressure P_p . At the same time, the normal faults are slowly loaded due to a combination of thermoelastic contraction and tectonic loading. Reservoir cooling and tectonic loading (secular strain rates in this region show areal dilation according to Kreemer et al. (2012)) would reduce the minimum horizontal principal stress (S_{hmin}) and thus enhance the differential stress loaded on the normal fault if the vertical principal stress stays constant in time. This reduces P_{crit} according to Equation 5. The seismicity is inhibited (Figure 2), indicating that P_p remains below P_{crit} (Figure 10).

The only exception is in a small area to the southeast of the main seismicity cluster, where most of the MSEs during normal operations occurred (Figure 7). This small area is associated with the lowest Vp values (2.8–3.0 km/s) (Figure 7). This might be caused by locally higher P_p and/or increased rock damage, which would result in P_p exceeding P_{crit} there.

During shutdown, P_p recovers rapidly and exceeds P_{crit} , inducing microseismicity (Figure 10, gray shaded area). After production resumes, P_{crit} decreases at a similar rate as before shutdown due to reduced S_{hmin} whereas P_p decreases more quickly to a value less than P_{crit} , inhibiting microseismicity.

5.4. Possible Correlation Between Pore Pressure and Event Magnitude

As shown in Figures 3c and 3d, during shutdown the larger magnitude events tend to be located closer to the production wells. The hydrologic modeling study also shows that the P_p increase is higher near the production wells during pumping cessation (Feigl et al., 2022). This suggests that there may be a positive correlation between P_p increase and event magnitude. Seismic events with higher shear modulus, larger slip area, and/or larger slip distance will have higher magnitudes. The proportion of a fault plane reaching critical shear stress will be larger if the P_p increase is larger, leading to a greater likelihood of rupturing a larger slip patch and thereby generating a larger-magnitude seismic event. Thus, we suggest that the observed correlation between MSE magnitude and the distance to the production wells may be due to the spatial variation in P_p increase around the production wells during pumping cessation. A similar phenomenon has also been observed at The Geysers in California by Martínez-Garzón, Kwiatek, Sone, et al. (2014) who found that the cumulative seismic moment released by seismicity increased during peak injection periods due to the occurrence of larger maximum magnitude events.

6. Conclusion

We have performed detailed seismic and stress analysis with data from a dense seismic array to characterize the geothermal reservoir at San Emidio, Nevada, where a substantial increase in microseismicity during a plant shutdown in December 2016 was observed. The seismic events are very small with coda duration magnitudes ranging from -2.2 to 0 . Our MSE relocations show that the main seismicity cluster is linearly distributed on the westward dipping BBF and most of the other MSEs likely occurred on small-scale fractures near and between existing normal faults. Our tomographic Vp model shows that the fault patches and fractures delineated by MSEs are within a low-velocity body, which is in contact with the perforated sections of nearby active production wells. Focal mechanisms are dominated by normal faulting with some strike-slip components and have a wide

range of orientations, consistent with the normal faulting stress regime. Given the local stress state, the BBF hosting the main seismicity cluster is optimally oriented for failure. Spatial variations in the local stress state are also observed, indicating stress heterogeneity in the reservoir. These results combine to indicate that the geothermal reservoir at San Emidio is a fractured, fluid-filled, and permeable body that has developed along the existing normal faults. We suggest that the MSEs during plant shutdown at San Emidio occurred on pre-existing, small-scale, critically stressed fault patches and fractures in the reservoir, which were activated due to increased P_p and decreased effective normal stress around the wells when the production pumping ceased. We suggest that long-term reductions in P_{crit} during normal production operations (possibly caused by reservoir cooling, tectonic loading, or some other process) play important roles in a critically stressed reservoir. The observed correlation between the magnitudes of the MSEs and their distances to the production wells may be due to the spatial variation in P_p increase around the production wells during pumping cessation.

Data Availability Statement

Seismic data collection was completed at San Emidio in late 2016 by Microseismic Inc. as part of U.S. Department of Energy project number DE-EE0007698 as described at <https://gdr.openei.org/submissions/1386> (Lord et al., 2016a). The raw seismic data, well positions, and pumping data have been deposited in the U.S. Department of Energy's Geothermal Data Repository. The raw seismic data are available at <https://gdr.openei.org/submissions/1395> (Lord et al., 2016b). The well positions are available at <https://gdr.openei.org/submissions/1551> (Cardiff et al., 2023a). The production and injection pumping data are available at <https://gdr.openei.org/submissions/1552> (Cardiff et al., 2016). The focal mechanism inversion software HASH (v1.2) is available at <https://www.usgs.gov/node/279393> (Hardebeck & Shearer, 2002). The stress inversion software MSATSI (v1.0.10) is available at <http://induced.pl/msatsi> (Martínez-Garzón, Kwiatek, Ickrath, & Bohnhoff, 2014). The seismic event catalog, containing event origin times, relocations, magnitudes, and focal mechanisms, and the 3-D Vp model that we determined in this study, are provided in Tables S1 and S2, respectively (Table captions are in Supporting Information S1).

Acknowledgments

We thank the editor, associate editor, and an anonymous reviewer whose comments greatly improved the manuscript. We thank Michael Cardiff and Herbert F. Wang for their helpful discussions and comments. We thank Ken Smith from the Nevada Seismological Laboratory for providing the coda duration magnitude equation. The WHOLES-scale team thanks the following individuals at Ormat Technologies: Curtis Peach, Cliff Reed, Joe Pavone, Manolo Di Donato, Leeta Miller, Alan Pinuelas-Molina, David Schwab, Lupé Gonzalez Ortiz, Gabrielle Ramirez, Courtney Brailo, Zack Young, John Murphy, and Robin Zuza. Most figures were made with The Generic Mapping Tools version 6 (GMT 6, Wessel et al., 2019). The work presented herein has been funded in part by the Office of Energy Efficiency and Renewable Energy (EERE), U.S. Department of Energy, under Award Numbers DE-EE0007698 and DE-EE0009032.

References

- Cardiff, M., Akerley, J., & Feigl, K. L. (2016). WHOLES-scale: Mass flux rates for wells at San Emidio in December 2016 [Dataset]. U.S. Department of Energy's Geothermal Data Repository. <https://doi.org/10.15121/2006850>
- Cardiff, M., Akerley, J., & Feigl, K. L. (2023a). WHOLES-scale: Coordinates of wells at San Emidio, Nevada [Dataset]. U.S. Department of Energy's Geothermal Data Repository. <https://doi.org/10.15121/2006837>
- Cardiff, M., Lim, D. D., Patterson, J. R., Akerley, J., Spielman, P., Lopeman, J., et al. (2018). Geothermal production and reduced seismicity: Correlation and proposed mechanism. *Earth and Planetary Science Letters*, 482, 470–477. <https://doi.org/10.1016/j.epsl.2017.11.037>
- Cardiff, M. A., Sherman, C., Guo, H., Cunningham, E., Folsom, M., Murphy, J., et al. (2023b). WHOLES-scale—Calibration and simulation of hydro-mechanical behavior at San Emidio, Nevada during operational changes. In *Proceedings, 48th workshop on geothermal reservoir engineering*. Stanford University. SGP-TR-224. Retrieved from <https://pangea.stanford.edu/ERE/db/GeoConf/papers/SGW/2023/Cardiff.pdf>
- Chen, C., & Holland, A. A. (2016). PhasePapy: A robust pure Python package for automatic identification of seismic phases. *Seismological Research Letters*, 87(6), 1384–1396. <https://doi.org/10.1785/0220160019>
- Efron, B., & Gong, G. (1983). A leisurely look at the bootstrap, the jackknife, and cross-validation. *The American Statistician*, 37(1), 36–48. <https://doi.org/10.1080/00031305.1983.10483087>
- Efron, B., & Tibshirani, R. (1991). Statistics data analysis in the computer age. *Science*, 253(5018), 390–395. <https://doi.org/10.1126/science.253.5018.390>
- Ellsworth, W. L. (2013). Injection-induced earthquakes. *Science*, 341(6142), 1225942. <https://doi.org/10.1126/science.1225942>
- Feigl, K. L., Guo, H., Cunningham, E., Hampton, J., Folsom, M., Akerley, J., et al. (2023). The 2022 WHOLES-scale deployment at San Emidio, Nevada, US. In *Proceedings, 48th workshop on geothermal reservoir engineering*. Stanford University. SGP-TR-224. Retrieved from <https://pangea.stanford.edu/ERE/db/GeoConf/papers/SGW/2023/Feigl.pdf>
- Feigl, K. L., Tung, S., Guo, H., Cunningham, E., Hampton, J., Kleich, S. J., et al. (2022). Overview and preliminary results from the WHOLES-scale project at San Emidio, Nevada, US. In *Proceedings, 47th workshop on geothermal reservoir engineering*. Stanford University. SGP-TR-223. Retrieved from <https://pangea.stanford.edu/ERE/db/GeoConf/papers/SGW/2022/Feigl.pdf>
- Folsom, M., Libbey, R., Feucht, D., Warren, I., & Garanzini, S. (2020). Geophysical observations and integrated conceptual models of the San Emidio geothermal field, Nevada. In *Proceedings, 45th workshop on geothermal reservoir engineering*. Stanford University. SGP-TR-216. Retrieved from <https://pangea.stanford.edu/ERE/db/GeoConf/papers/SGW/2020/Folsom.pdf>
- Gonzalez, L. F., Aguiar, A. C., & Karplus, M. (2022). Data mining microseismicity associated to the Blue Mountain geothermal site. In *Proceedings, 47th workshop on geothermal reservoir engineering*. Stanford University. SGP-TR-223. Retrieved from <https://pangea.stanford.edu/ERE/db/GeoConf/papers/SGW/2022/Gonzalez1.pdf>
- Guo, H., McGuire, J. J., & Zhang, H. (2021). Correlation of porosity variations and rheological transitions on the southern Cascadia megathrust. *Nature Geoscience*, 14(5), 341–348. <https://doi.org/10.1038/s41561-021-00740-1>
- Guo, H., & Zhang, H. (2017). Development of double-pair double difference earthquake location algorithm for improving earthquake locations. *Geophysical Journal International*, 208(1), 333–348. <https://doi.org/10.1093/gji/ggw397>
- Guo, H., Zhang, H., & Froment, B. (2018). Structural control on earthquake behaviors revealed by high-resolution Vp/Vs imaging along the Gofar transform fault, East Pacific Rise. *Earth and Planetary Science Letters*, 499, 243–255. <https://doi.org/10.1016/j.epsl.2018.07.037>

- Hardebeck, J. L., & Michael, A. J. (2006). Damped regional-scale stress inversions: Methodology and examples for southern California and the Coalinga aftershock sequence. *Journal of Geophysical Research*, *111*(B11), B11310. <https://doi.org/10.1029/2005JB004144>
- Hardebeck, J. L., & Shearer, P. M. (2002). A new method for determining first-motion focal mechanisms. *Bulletin of the Seismological Society of America*, *92*(6), 2264–2276. <https://doi.org/10.1785/0120010200>
- Heidbach, O., Rajabi, M., Cui, X., Fuchs, K., Müller, B., Reinecker, J., et al. (2018). The world stress map database release 2016: Crustal stress pattern across scales. *Tectonophysics*, *744*, 484–498. <https://doi.org/10.1016/j.tecto.2018.07.007>
- Herrmann, R. B. (1975). The use of duration as a measure of seismic moment and magnitude. *Bulletin of the Seismological Society of America*, *65*(4), 899–913. <https://doi.org/10.1785/BSSA0650040899>
- Hutchings, L., Bonner, B., Saltiel, S., Jarpe, S., & Nelson, M. (2019). Rock physics interpretation of tomographic solutions for geothermal reservoir properties. In *Applied geophysics with case studies on environmental, exploration and engineering geophysics*. IntechOpen: Ali Ismet Kanli. <https://doi.org/10.5772/intechopen.81226>
- Jahnke, B., Sone, H., Guo, H., Sherman, C., Warren, I., Kreemer, C., et al. (2023). Geomechanical analysis of the geothermal reservoir at San Emidio, Nevada. *Geothermics*, *110*, 102683. <https://doi.org/10.1016/j.geothermics.2023.102683>
- Keranan, K. M., & Weingarten, M. (2018). Induced seismicity. *Annual Review of Earth and Planetary Sciences*, *46*(1), 149–174. <https://doi.org/10.1146/annurev-earth-082517-010054>
- Kilb, D., & Hardebeck, J. L. (2006). Fault parameter constraints using relocated earthquakes: Validation of first motion focal mechanism data. *Bulletin of the Seismological Society of America*, *96*(3), 1140–1158. <https://doi.org/10.1785/0120040239>
- Koper, K. D., Holt, M. M., Voyles, J. R., Burlacu, R., Pyle, M. L., Wang, R., & Schmandt, B. (2020). Discrimination of small earthquakes and buried single-fired chemical explosions at local distances (<150 km) in the western United States from comparison of local magnitude (M_L) and coda duration magnitude (M_C). *Bulletin of the Seismological Society of America*, *111*(1), 558–570. <https://doi.org/10.1785/0120200188>
- Kreemer, C., Hammond, W. C., Blewitt, G., Holland, A. A., & Bennett, R. A. (2012). *A geodetic strain rate model for the Pacific-North American plate boundary, western United States, Map 178, scale 1:1,500,000*. Nevada Bureau of Mines and Geology.
- Lee, W. H. K., Bennett, R. E., & Meagher, K. L. (1972). *A Method of estimating magnitude of local earthquakes from signal duration (Open File Report)* (p. 28). U.S. Geological Survey. Retrieved from <https://pubs.usgs.gov/of/1972/0223/report.pdf>
- Lord, N., Heath, B., Guo, H., Warren, I., Bradshaw, S., Thurber, C. H., et al. (2016a). Seismic Survey 2016 metadata at San Emidio, Nevada, United States [Dataset]. U.S. Department of Energy's Geothermal Data Repository. <https://doi.org/10.15121/1872549>
- Lord, N., Heath, B., Guo, H., Warren, I., Bradshaw, S., Thurber, C. H., et al. (2016b). Seismic Survey 2016 data at San Emidio Nevada, United States [Dataset]. U.S. Department of Energy's Geothermal Data Repository. <https://doi.org/10.15121/2008357>
- Maeda, N. (1985). A method for reading and checking phase times in auto-processing system of seismic wave data. *Zisin*, *38*(3), 365–379. https://doi.org/10.4294/zisin1948.38.3_365
- Martínez-Garzón, P., Kwiatak, G., Ickrath, M., & Bohnhoff, M. (2014). MSATSI: A MATLAB package for stress inversion combining solid classic methodology, a new simplified user-handling, and a visualization tool. *Seismological Research Letters*, *85*(4), 896–904. <https://doi.org/10.1785/0220130189>
- Martínez-Garzón, P., Kwiatak, G., Sone, H., Bohnhoff, M., Dresen, G., & Hartline, C. (2014). Spatiotemporal changes, faulting regimes, and source parameters of induced seismicity: A case study from the Geysers geothermal field. *Journal of Geophysical Research: Solid Earth*, *119*(11), 8378–8396. <https://doi.org/10.1002/2014JB011385>
- Pechmann, J. C., Bernier, J. C., Nava, S. J., & Terra, F. M. (2006). Correction of systematic time-dependent coda magnitude errors in the Utah and Yellowstone National Park region earthquake catalogs, 1981–2001. In W. J. Arabasz, R. B. Smith, J. C. Pechmann, K. L. Pankow, & R. Burlacu (Eds.), *Integrated regional and urban seismic monitoring—Wasatch front area, Utah and adjacent Intermountain seismic belt, Appendix C, U.S. Geologic Survey: Final technical report cooperative agreement 04HQAG0014* (p. 137). Retrieved from https://earthquake.usgs.gov/cfusion/external_grants/reports/04HQAG0014.pdf
- Rhodes, G. T. (2011). Structural controls of the San Emidio geothermal system, northwestern Nevada. (Master's thesis). University of Nevada. Retrieved from ScholarWorks. Retrieved from <http://scholarworks.unr.edu:8080/handle/11714/4011>
- Rhodes, G. T., Faulds, J. E., & Ramelli, A. R. (2011). *Preliminary geologic map of the northern lake range, San Emidio geothermal area, Washoe County, Nevada (open file report, 11-11)*. Nevada Bureau of Mines and Geology.
- Rubin, A. M., Gillard, D., & Got, J. L. (1999). Streaks of microearthquakes along creeping faults. *Nature*, *400*(6745), 635–641. <https://doi.org/10.1038/23196>
- Schaff, D. P., Bokelmann, G. H., Ellsworth, W. L., Zankerka, E., Waldhauser, F., & Beroza, G. C. (2004). Optimizing correlation techniques for improved earthquake location. *Bulletin of the Seismological Society of America*, *94*(2), 705–721. <https://doi.org/10.1785/0120020238>
- Segall, P. (1989). Earthquakes triggered by fluid extraction. *Geology*, *17*(10), 942–946. [https://doi.org/10.1130/0091-7613\(1989\)017<0942:ETBFE>2.3.CO;2](https://doi.org/10.1130/0091-7613(1989)017<0942:ETBFE>2.3.CO;2)
- Segall, P., & Fitzgerald, S. D. (1998). A note on induced stress changes in hydrocarbon and geothermal reservoirs. *Tectonophysics*, *289*(1–3), 117–128. [https://doi.org/10.1016/S0040-1951\(97\)00311-9](https://doi.org/10.1016/S0040-1951(97)00311-9)
- Sicking, C., Vermilye, J., Geiser, P., Lacazette, A., & Thompson, L. (2012). *Permeability field imaging from microseismic* (pp. 1–5). SEG Technical Program Expanded Abstracts. <https://doi.org/10.1190/segam2012-1383.1>
- Templeton, D. C., Matzel, E. M., & Cladouhos, T. T. (2017). Evolution of microseismicity at the Blue Mountain geothermal site. *Geothermal Resources Council Annual Meeting Transactions*, *41*. <https://publications.mygeoenergynow.org/grc/1033836.pdf>
- Tosha, T., Sugihara, M., & Nishi, Y. (1998). Revised hypocenter solutions for microearthquakes in the Kakkonda geothermal field, Japan. *Geothermics*, *27*(5–6), 553–571. [https://doi.org/10.1016/S0375-6505\(98\)00033-9](https://doi.org/10.1016/S0375-6505(98)00033-9)
- Vavryčuk, V. (2014). Iterative joint inversion for stress and fault orientations from focal mechanisms. *Geophysical Journal International*, *199*(1), 69–77. <https://doi.org/10.1093/gji/ggu224>
- Waldhauser, F., & Ellsworth, W. L. (2000). A double-difference earthquake location algorithm: Method and application to the northern Hayward fault, California. *Bulletin of the Seismological Society of America*, *90*(6), 1353–1368. <https://doi.org/10.1785/0120000006>
- Waldhauser, F., Ellsworth, W. L., Schaff, D. P., & Cole, A. (2004). Streaks, multiplets, and holes: High-resolution spatio-temporal behavior of Parkfield seismicity. *Geophysical Research Letters*, *31*(18). <https://doi.org/10.1029/2004GL020649>
- Warren, I., Gasperikova, E., Pullamannappallil, S., & Grealy, M. (2018). Mapping geothermal permeability using passive seismic emission tomography constrained by cooperative inversion of active seismic and electromagnetic data. In *Proceedings, 43rd workshop on geothermal reservoir engineering*. Stanford University. SGP-TR-213. Retrieved from <https://pangea.stanford.edu/ERE/pdf/IGASstandard/SGW/2018/Warren.pdf>
- Wessel, P., Luis, J. F., Uieda, L., Scharroo, R., Wobbe, F., Smith, W. H. F., & Tian, D. (2019). The generic mapping tools version 6. *Geochemistry, Geophysics, Geosystems*, *20*(11), 5556–5564. <https://doi.org/10.1029/2019GC008515>

- Winkler, K., & Nur, A. (1979). Pore fluids and seismic attenuation in rocks. *Geophysical Research Letters*, 6(1), 1–4. <https://doi.org/10.1029/GL006i001p00001>
- Zang, A., Oye, V., Jousset, P., Deichmann, N., Gritto, R., McGarr, A., et al. (2014). Analysis of induced seismicity in geothermal reservoirs—An overview. *Geothermics*, 52, 6–21. <https://doi.org/10.1016/j.geothermics.2014.06.005>
- Zelt, C. A. (1998). Lateral velocity resolution from three-dimensional seismic refraction data. *Geophysical Journal International*, 135(3), 1101–1112. <https://doi.org/10.1046/j.1365-246X.1998.00695.x>
- Zhang, H., & Thurber, C. H. (2003). Double-difference tomography: The method and its application to the Hayward fault, California. *Bulletin of the Seismological Society of America*, 93(5), 1875–1889. <https://doi.org/10.1785/0120020190>
- Zhang, H., & Thurber, C. H. (2006). Development and applications of double-difference seismic tomography. *Pure and Applied Geophysics*, 163(2), 373–403. <https://doi.org/10.1007/s00024-005-0021-y>
- Zoback, M. D. (2007). *Reservoir geomechanics*. Cambridge University Press.